Scattering from Time-Modulated Transmission-Line Loads: Theory and Experiments in Acoustics

Matthieu Malléjac[*] and Romain Fleury[†]

Laboratory of Wave Engineering, École Polytechnique Fédérale de Lausanne, Switzerland

Scattering wave systems that are periodically modulated in time offer many new degrees of freedom to control waves in both the spatial and frequency domains. Such systems, albeit linear, do not conserve frequency and require the adaptation of the usual theories and methods. In this paper, we provide a general extension of transmission-line or telegraph equations to periodically time-modulated systems. As a byproduct of the theory, we obtain a general approach to compute and measure the complete scattering matrix of such systems. Finally, the proposed theory and methods are applied and validated on a concrete practical example in the realm of airborne acoustics: a time-modulated actively controlled loudspeaker membrane terminating a monomode waveguide. Different modulation functions and parameters are tested. The experimental results are compared to both numerical simulation and an analytical model based on a two-time-scale method.

I. INTRODUCTION

Time-varying wave media have attracted a great deal of interest over the past few decades and have opened new perspectives in the field of metamaterials by adding a new degree of freedom in wave manipulation and engineering possibilities [1]. The first studies on wave propagation in time-varying media date back to the work of Morgenthaler [2], Felsen *et al.* [3], and Fante [4] on spatially homogeneous but time-varying dielectric and dispersive media. Scattering from temporal boundary conditions and discontinuities gives rise to intriguing phenomena. The temporal dual of wave scattering on a planar interface between two media cannot, due to causality, involve a reflection to negative times, thus leading to different Fresnel coefficients. Another important contrast between spatial and temporal crystals or metamaterials, i.e., a slab of (locally resonant) medium varying periodically in time, is the fact that they can generate not only frequency band gaps, but also wavenumber gaps, corresponding to linearly unstable regimes [5].

In particular, systems that are periodically modulated in time, or time-Floquet systems, have the ability to alleviate some of the constraints of simple static media [6], such as the breaking of time-reversal symmetry and of reciprocity [7–9]. As a result, exciting possibilities for wave control open, such as magnet-free circulators

and temporal aiming [10,11], Floquet topological insulators [12–15], unidirectional and parametric amplification [16–25], frequency conversion [25–27], holography [28], near-zero-index-enabled behaviors (negative refraction, high harmonic generation, time reversal, broadband, and controllable frequency shift) [29–33], or strong nonlinear behavior [34] allowing the observation of Floquet solitons [35] or the development of wave-based neuromorphic computing [36]. One of the main characteristics of Floquet metamaterials is the generation of harmonics at integer multiples of the modulation frequency, thus requiring an adaptation of classical experimental or theoretical methods where natural hypotheses such as linearity, reciprocity, and frequency conservation are assumed.

Many efforts have already been made to theoretically describe time-varying systems [37,38] and their components [39] as well as to extend theoretical tools such as the generalization of Kramers-Kronig relations [40], of particle's dipolar polarizability [41], of the transfer-matrix methods [42], or of the T matrix [43], among others. The transmission line is another key concept fundamental to wave engineering, as it allows for the characterization of wave systems involving the scattering of guided waves. From this theory, one can describe and define the scattering of N-port systems, and easily connect several scatterers together to compose more complex systems. The growing interest in time-varying media requires this theory to be extended to multiharmonic systems, from both theoretical and experimental points of view.

In this paper, we provide a comprehensive framework to explore the guided-wave scattering of time-modulated

————————
[*]matthieu.mallejac@epfl.ch
[†]romain.fleury@epfl.ch

loads, from theory to experiments. In particular, the measurement of the complete scattering matrix of such systems, including potential Floquet harmonics, remains an experimental challenge, for which we propose a solution.

The paper is structured as follows. In a first section, we derive and expose the extended theory of transmission-line, scattering and reduced-impedance matrices, for time-modulated systems. In a second section, we present a method for extracting the complete scattering matrix based on a multiload technique. These two sections are general and can be applied to several domains of wave physics (electrical, acoustic or mechanical transmission lines, for example). Finally, we take an acoustic example to apply the theory on a concrete case, and demonstrate experimentally our *S*-matrix extraction method: an actively controlled loudspeaker with an assigned input impedance modulated in time. Analytical modeling based on a two-time-scale method and numerical simulations are used to confirm the experimental results obtained for different modulation functions and parameters.

II. TIME-MODULATED TRANSMISSION-LINE THEORY

We consider here a very general one-dimensional transmission line where x and y can represent any quantities such that, in the static case, the two are related by the impedance $Z(\omega)$:

$$x(z,\omega) = Z(z,\omega)y(z,\omega). \tag{1}$$

For electrical, acoustic, or mechanical circuits, x is, respectively, the voltage U, the pressure P, or the force F, while y is the current intensity I, the particle velocity V, or the velocity V. The transmission line is terminated by a time-varying load, $Z_t(t)$, as shown in Fig. 1.

A. Constant load

We first recall some well-known generalities about transmission lines where the termination load does not vary with time [44]. In this case, the scalar fields at position z can be written as the superposition of the incident x_i and reflected x_r waves. Denoting the characteristic impedance of the line by Z_0, one has

$$x(z,\omega) = x_i(z,\omega) + x_r(z,\omega), \tag{2}$$

$$y(z,\omega) = \frac{x_i(z,\omega) - x_r(z,\omega)}{Z_0}, \tag{3}$$

which can be related by a scalar scattering coefficient at $z = 0$,

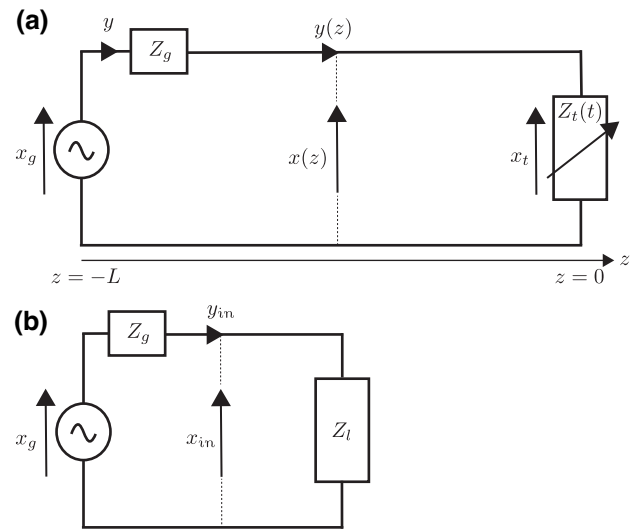$$x_r(z = 0, \omega) = S_t x_i(z = 0, \omega), \tag{4}$$

FIG. 1. Transmission-line circuit terminated by a time-modulated load (a), and reduced-impedance circuit (b).

i.e., the complex reflection coefficient $S_t = R$. Alternatively, the scalar impedance of the load can be related to the reflection coefficient as

$$S_t = R = \frac{Z_t/Z_0 - 1}{Z_t/Z_0 + 1}, \tag{5}$$

or, equivalently,

$$Z_t = Z(z = 0) = Z_0 \frac{1 + R}{1 - R}. \tag{6}$$

B. Periodically time-modulated load

If the load is now modulated periodically in time with a circular frequency ω_m, Floquet harmonics at $\omega \pm n\omega_m$ ($n \in \mathbb{N}$) are generated around the excitation frequency ω and will be reflected from the load. Moreover, since in the general case the source is not impedance-matched, the multiharmonic reflection from the load will also be reflected back from the generator side. Both the incident and the reflected waves can therefore be developed in Fourier series. Since the amplitudes of the harmonics must decrease at large n, we can always truncate their summation to a given harmonic order N, approximating the signals as follows:

$$x(z,t) = \sum_{n=-N}^{N} \mathbf{x}[n](z)e^{i(\omega + n\omega_m)t}, \tag{7}$$

$$y(z,t) = \sum_{n=-N}^{N} \mathbf{y}[n](z)e^{i(\omega + n\omega_m)t}. \tag{8}$$

Here $\mathbf{x}[n](z)$ and $\mathbf{y}[n](z)$ are the nth elements of the complex amplitude vectors $\mathbf{x}(z)$ and $\mathbf{y}(z)$ of length $2N + 1$, respectively, defined at each position z.

As a generalization of Eqs. (2)–(4), these complex amplitudes can be expressed as

$$\mathbf{x}(z) = \mathbf{x}_i(z) + \mathbf{x}_r(z) = [\mathbb{1} + \mathbf{S}(z)] \cdot \mathbf{x}_i(z), \qquad (9)$$

$$\mathbf{y}(z) = \frac{\mathbf{x}_i(z) - \mathbf{x}_r(z)}{Z_0} = [\mathbb{1} - \mathbf{S}(z)] \cdot \frac{\mathbf{x}_i(z)}{Z_0}, \qquad (10)$$

using the matrix generalization of the scattering coefficient, Eq. (4).

The incident and reflected complex amplitude vectors can be expressed as the elementwise multiplication of a magnitude vector $\mathbf{x}_{i,r}^{\mathrm{abs}}$ and a phase vector $\mathbf{d}(z)$,

$$\mathbf{x}_{i,r}(z) = \mathbf{x}_{i,r}^{\mathrm{abs}} \odot \mathbf{d}(z), \qquad (11)$$

where the magnitude vector is given by $\mathbf{x}_{i,r}^{\mathrm{abs}} = [|x_{i,r}^{(-N)}|, \ldots, |x_{i,r}^{(0)}|, \ldots, |x_{i,r}^{(+N)}|]^T$. The phase vector is defined as $\mathbf{d}(z) = [e^{ik^{(-N)}z}, \ldots, e^{ik^{(0)}z}, \ldots, e^{ik^{(+N)}z}]^T$, with the wavenumbers $k^{(n)} = (\omega \pm n\omega_m)/c_0$. The wave celerity in the line is $c_0 = \mathrm{const}$. The operator $\odot$ is the Hadamard product, i.e., the elementwise multiplication operator.

Because of the multiharmonic content, Eqs. (5) and (6) also need to be generalized. What used to be the scalar scattering coefficient and impedance now become $(2N + 1)$ by $(2N + 1)$ matrices, related by

$$\mathbf{Z}_t = \mathbf{Z}(z = 0) = Z_0 [\mathbb{1} + \mathbf{S}_t] \cdot [\mathbb{1} - \mathbf{S}_t]^{-1}, \qquad (12)$$

$$\mathbf{S}_t = \left[\mathbb{1} + \frac{\mathbf{Z}_t}{Z_0}\right]^{-1} \cdot \left[\frac{\mathbf{Z}_t}{Z_0} - \mathbb{1}\right]. \qquad (13)$$

These relations can be easily derived by introducing Eqs. (9) and (10), in the matrix extended definition of the impedance and scattering coefficient at the load position:

$$\mathbf{x}(z = 0) = \mathbf{Z}_t \cdot \mathbf{y}(z = 0), \qquad (14)$$

$$\mathbf{x}_r(z = 0) = \mathbf{S}_t \cdot \mathbf{x}_i(z = 0). \qquad (15)$$

We can then determine the scattering and impedance matrices at any z position along the transmission line from those at the termination. The reduced impedance can be expressed as

$$\mathbf{Z}(z) = Z_0 \left[\mathbb{1} + \left[\left[\mathbb{1} + \frac{\mathbf{Z}_t}{Z_0}\right]^{-1} \cdot \left[\frac{\mathbf{Z}_t}{Z_0} - \mathbb{1}\right]\right.\right.$$

$$\odot \left(\mathbf{d}(z) \cdot \mathbf{d}(z)^T\right)\right]$$

$$\cdot \left[\mathbb{1} - \left[\mathbb{1} + \frac{\mathbf{Z}_t}{Z_0}\right]^{-1} \cdot \left[\frac{\mathbf{Z}_t}{Z_0} - \mathbb{1}\right]\right.$$

$$\left.\left.\odot \left(\mathbf{d}(z) \cdot \mathbf{d}(z)^T\right)\right]^{-1}, \qquad (16)$$

and the scattering matrix reduced to the z position is given by $\mathbf{S}(z) = \mathbf{S}_t \odot \left(\mathbf{d}(z) \cdot \mathbf{d}(z)^T\right)$.

Finally, we can compute the average power along the transmission line as

$$\mathscr{P}(z) = \frac{1}{2} \mathrm{Re}\{\mathbf{x} \cdot \mathbf{y}^*\} = [\mathbb{1} + \mathbf{S}(z)] \cdot \left[\mathbf{x}_i^{\mathrm{abs}} \odot \mathbf{d}^*(z)\right]$$

$$\cdot [\mathbb{1} - \mathbf{S}(z)]^* \cdot \frac{\mathbf{x}_i^{\mathrm{abs}} \odot \mathbf{d}(z)}{Z_0}. \qquad (17)$$

In terms of incident $\mathscr{P}_i$ and reflected $\mathscr{P}_r$ power, we have

$$\mathscr{P}(z) = \mathscr{P}_i(z) + \mathscr{P}_r(z) = \frac{1}{2Z_0}|\mathbf{x}_i|^2 - \frac{1}{2Z_0}|\mathbf{S}(z) \cdot \mathbf{x}_i|^2. \qquad (18)$$

According to Fig. 1(b), the incident wave can also be defined with respect to the generator voltage, pressure, or force through the load impedance reduced to the generator position,

$$\mathbf{x}_{\mathrm{in}} = \mathbf{Z}_{\mathrm{in}} \cdot [\mathbf{Z}_s + \mathbf{Z}_{\mathrm{in}}]^{-1} \cdot \mathbf{x}_g$$

$$= [\mathbb{1} + \mathbf{S}(-L)] \cdot \mathbf{x}_i^{\mathrm{abs}} \odot \mathbf{d}^*(-L), \qquad (19)$$

with the input impedance $\mathbf{Z}_{\mathrm{in}}$ being defined from Eq. (16),

$$\mathbf{Z}_{\mathrm{in}} = \mathbf{Z}(-L). \qquad (20)$$

These equations provide, from the measured time signals $x(t)$ and/or $y(t)$ developed in Fourier series, the total field at each Floquet harmonic, $\mathbf{x}$ and $\mathbf{y}$, and allow one to fully characterize a time-modulated load in terms of scattering, impedance, and power.

III. EXTRACTION OF THE SCATTERING MATRIX

Extracting the complete scattering matrix of a time-modulated system remains a challenge due to the multiharmonic content. One needs to measure $2N + 1$ linearly independent data sets from which one can extract any of the elements of the $\mathbf{S}_t$ matrix.

Here, we propose a general methodology based on multiload techniques [45] to measure the $(2N + 1)$ by $(2N + 1)$ scattering matrix while limiting the number of sensors required. It is worth noting here that another method would consist in multiplying the number of sensors in the system.

Two extraction methods can be employed. First, $\mathbf{S}_t$ can be extracted by probing $x(t)$ at two positions in the transmission line, which allows one to differentiate the incident $\mathbf{x}_i$ and reflected $\mathbf{x}_r$ fields for each harmonic that are related to $\mathbf{S}_t$ through Eq. (15). For the second method, we can use Eq. (12) to obtain $\mathbf{S}_t$ from the $\mathbf{Z}_t$ matrix that relates the harmonic content of the $x(t)$ and $y(t)$ fields measured at the load position [Eq. (14)].

A. Multiload technique

Both methods involve inverting equations with vectors. To do this, we expand the vectors $\mathbf{x}_i$ and $\mathbf{x}_r$, or $\mathbf{x}$ and $\mathbf{y}$, into square matrices, multiplying the number of measurements, thus multiplying the number of equations, to solve for the $(2N + 1)^2$ unknowns. In order to invert these matrices, the equations must be linearly independent in the frequency range of interest. We can then vary the length of the transmission line between the load to be characterized and the probe position for each measurement. By doing so, we can change the phase of the reflected field at the microphone position. The length should be chosen so that each configuration gives independent data sets over the frequency range for $\mathbf{x}_i$ and $\mathbf{x}_r$, or $\mathbf{x}(z = 0)$ and $\mathbf{y}(z = 0)$. In addition, these methods assume plane-wave propagation. The excitation frequency as well as all generated Floquet harmonics must be lower than the waveguide cutoff frequency.

Equations (15) and (14) can then be rewritten as

$$
\mathbf{S}_t = \begin{bmatrix} x_{r_{L_1}}^{-N} & \cdots & x_{r_{L_{2N+1}}}^{-N} \\ \vdots & \ddots & \vdots \\ x_{r_{L_1}}^{0} & \cdots & x_{r_{L_{2N+1}}}^{0} \\ \vdots & \ddots & \vdots \\ x_{r_{L_1}}^{+N} & \cdots & x_{r_{L_{2N+1}}}^{+N} \end{bmatrix} \cdot \begin{bmatrix} x_{i_{L_1}}^{-N} & \cdots & x_{i_{L_{2N+1}}}^{-N} \\ \vdots & \ddots & \vdots \\ x_{i_{L_1}}^{0} & \cdots & x_{i_{L_{2N+1}}}^{0} \\ \vdots & \ddots & \vdots \\ x_{i_{L_1}}^{+N} & \cdots & x_{i_{L_{2N+1}}}^{+N} \end{bmatrix}^{-1}
\tag{21}
$$

and

$$
\mathbf{Z}_t = \begin{bmatrix} x_{L_1}^{-N} & \cdots & x_{L_{2N+1}}^{-N} \\ \vdots & \ddots & \vdots \\ x_{L_1}^{0} & \cdots & x_{L_{2N+1}}^{0} \\ \vdots & \ddots & \vdots \\ x_{L_1}^{+N} & \cdots & x_{L_{2N+1}}^{+N} \end{bmatrix}_{z=0} \cdot \begin{bmatrix} y_{L_1}^{-N} & \cdots & y_{L_{2N+1}}^{-N} \\ \vdots & \ddots & \vdots \\ y_{L_1}^{0} & \cdots & y_{L_{2N+1}}^{0} \\ \vdots & \ddots & \vdots \\ y_{L_1}^{+N} & \cdots & y_{L_{2N+1}}^{+N} \end{bmatrix}_{z=0}^{-1} .
\tag{22}
$$

The inversion of these square matrices is sensitive to the independence of the data sets, i.e., to the choice of the load lengths. Computing the condition number of the matrix to be inverted allows one to select adequate lengths correctly. Initially, different lengths can be chosen so that, for the midrange frequency, each produces a phase shift linearly distributed in the range $[0, \pi]$.

To increase the accuracy for each frequency in the band, one can also overdetermine the system by increasing the number of configurations to be measured to M, i.e., M of transmission-line lengths. One can then solve the pseudoinverse of a $(2N + 1)$ by (M) matrix with a least-mean-squares procedure, thus minimizing the uncertainties in the inversion process due to matrices that may be close to singularity at some frequencies, i.e., data sets that are not sufficiently independent.

B. S matrix from $\mathbf{x}_i$ and $\mathbf{x}_r$ discrimination

For each of the $2N + 1$ charges, the incident $x_i^{(\pm n)}$ and reflected $x_r^{(\pm n)}$ complex amplitudes can be discriminated from the total field $x^{(\pm n)}(z)$ at each harmonic using two carefully calibrated probes positioned at z_1 and z_2:

$$
\begin{bmatrix} x_i^{(\pm n)} & x_r^{(\pm n)} \end{bmatrix} = \begin{bmatrix} x^{(\pm n)}(z_1) & x^{(\pm n)}(z_2) \end{bmatrix}
$$
$$
\times \begin{bmatrix} e^{-ik^{(\pm n)}z_1} & e^{-ik^{(\pm n)}z_2} \\ e^{ik^{(\pm n)}z_1} & e^{ik^{(\pm n)}z_2} \end{bmatrix}^{-1} .
\tag{23}
$$

One can then access $\mathbf{S}_t$ from the $2N + 1$ vectors $\mathbf{x}_r$ and $\mathbf{x}_i$ concatenated in matrices, as detailed in Eq. (21). This approach assumes linearity along the transmission line, and requires that individual harmonics do not interact with each other during propagation. The sole interactions should occur at the load.

C. S matrix from Z matrix

The impedance matrix can be obtained directly by simultaneously probing, at the load position, the total fields $x^{(\pm n)}$ and $y^{(\pm n)}$ at each harmonic and for the $2N + 1$ charges,

$$
\mathbf{x}(z = 0) = \begin{bmatrix} x_{z=0}^{(-N)} \\ \vdots \\ x_{z=0}^{(0)} \\ \vdots \\ x_{z=0}^{(+N)} \end{bmatrix} = \mathbf{Z}_t \cdot \begin{bmatrix} y_{z=0}^{(-N)} \\ \vdots \\ y_{z=0}^{(0)} \\ \vdots \\ y_{z=0}^{(+N)} \end{bmatrix} = \mathbf{Z}_t \cdot \mathbf{y}(z = 0).
\tag{24}
$$

The scattering matrix can then be deduced from the impedance matrix by simply solving Eq. (12).

IV. APPLICATION TO A TIME-MODULATED ACTIVELY CONTROLLED LOUDSPEAKER

We now apply the general theory and the extraction procedure of the scattering matrix to an acoustic example.

A. Experimental setup

We consider a one-dimensional acoustic waveguide of circular cross section with diameter $d = 7.18$ cm terminated by an actively controlled loudspeaker enclosed in a cavity of volume $V_b = 1081.6$ cm^3 as depicted in Figs. 2(a) and 2(b). The waveguide is instrumented with two microphones to measure the incident and reflected pressures, and is excited from the left by a monochromatic wave of circular frequency ω.
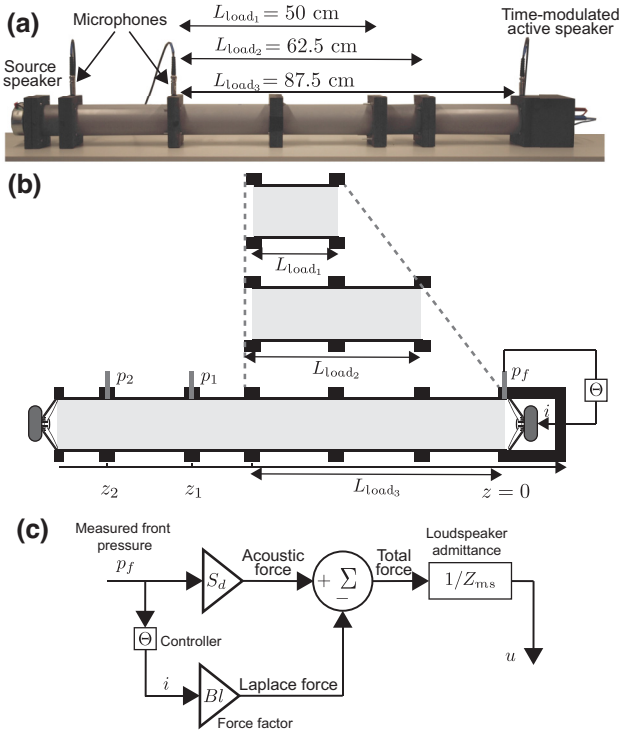
FIG. 2. Photograph (a) and schematic (b) of the experimental setup used to measure the entire scattering matrix of a time-modulated acoustic system. Block diagram (c) of the active control strategy.

With active control, the characteristics of a resonator, such as an electrodynamic loudspeaker, can differ completely from its natural properties, e.g., modified resonant frequency, stiffness, impedance [46], and nonlinearity, paving the way for a plethora of applications such as non-reciprocal behavior [47], gain and loss control [48,49], or enhanced broadband absorption [50–55], among others.

Here, we periodically modulate in time the impedance of the loudspeaker, so that it responds with a target impedance $Z_{\text{targ}}(t)$. The control part illustrated in Fig. 2(c), and performed using a field-programmable gate array–based (FPGA-based) Speedgoat Performance real-time controller (I/O 131), consists first in measuring the pressure p_f in front of the loudspeaker and then applying a feedback loop that assigns a given current $i(t)$ to the speaker, based on a given control law Θ:

$$i = \Theta p_f = \frac{S_d}{Bl}\left(1 - \frac{Z_{\text{ms}}(\omega_c)}{Z_{\text{targ}}(t)}\right)p_f. \qquad (25)$$

Here S_d is the speaker effective cross section, Bl is the force factor, and Z_{ms} is the specific impedance of the loudspeaker.

In the following, we will first consider a narrowband control, allowing the response of the resonator to time modulation to be carefully studied while decoupling the effect of the control at other frequencies. Apart from the narrow frequency range where the modulation occurs, no Floquet harmonics are generated. Only the middle column of the scattering matrix is thus meaningful, i.e., reflection at the different harmonics for incidence at the excitation frequency. Finally, we will demonstrate the experimental extraction of the full scattering matrix using a broadband control law, allowing the generation of harmonics for any excitation frequency and making the characterization of the complete matrix relevant.

B. Narrowband control

To limit the control over only a given bandwidth B_c around the control frequency f_c, a complex envelope technique based on a second-order Bessel function is adopted. More details on this technique and the control efficiency can be found in Ref. [46].

Two different periodic modulation functions are investigated in Figs. 3(a)–3(c), a cosine modulation, a positive circular modulation, and a negative circular modulation, respectively, such that

$$Z_{\text{targ}}(t) = Z_t\left(1 + A_m\cos(\omega_m t + \phi_m)\right) \qquad (26)$$

or

$$Z_{\text{targ}}(t) = Z_t\left(1 + A_m\exp(\pm i(\omega_m t + \phi_m))\right), \qquad (27)$$

where A_m, ϕ_m, and $\omega_m = 2\pi f_m$ are the modulation depth, phase, and circular frequency, respectively, and $\tilde{Z}_t = Z_t/Z_0$ is the amplitude of the target normalized impedance.

To characterize the effect of the modulation functions, the second column of the scattering matrix is extracted experimentally following the procedure detailed in Sec. III. In the following examples, the control characteristics are fixed as follows: $f_c = 220$ Hz, $B_c = 2$ Hz, $\tilde{Z}_t = 0.8$, $A_m = 0.2$, and $f_m = 50$ Hz. A prior pressure measurement along the transmission line ended by the time-modulated load showed that only the first Floquet harmonic is measurable in the system. Thus, the truncation in the Fourier series is set as $N = 1$.

Because of the control, the reflection at ω for an incidence at ω exhibits that of the natural loudspeaker, except in the control bandwidth around $f_c = 220$ Hz, where the reflection reaches the value given by the target impedance $|R| = |(\tilde{Z}_t - 1)/(1 + \tilde{Z}_t)|$, as shown in Figs. 3(a)–3(c-2). This is also the case for a time-invariant control, except that all the extra-diagonal terms of the matrix $\mathbf{S}_t$ are in this case null. Nonzero off-diagonal terms appear only when time modulation is enabled. In addition to the change in the reflection $|R^{(0,0)}|$ in the control range, it generates some reflection at the ± 1 Floquet harmonics. For example, two reflection peaks centered on f_c are now visible in Figs. 3(a-1) and 3(a-3), corresponding, respectively, to a
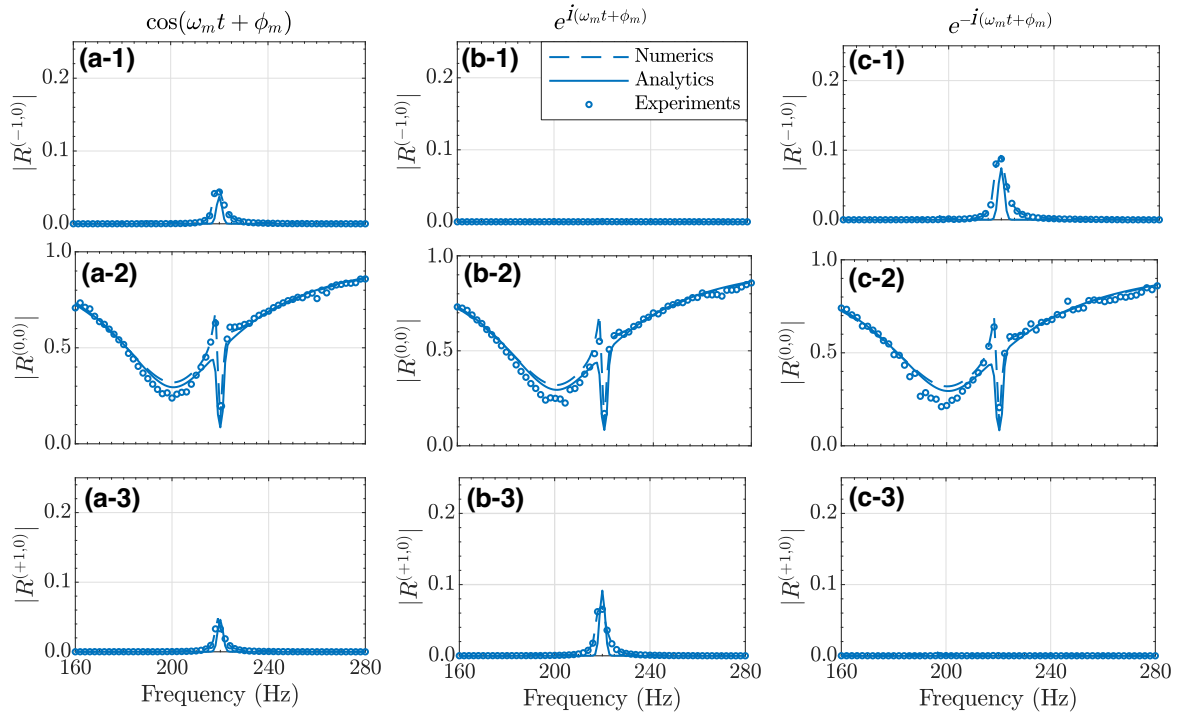
FIG. 3. Effect of the modulation function: the second column of the full scattering matrix for a cosine modulation (a), positive circular modulation (b), and negative circular modulation (c). The first, second, and third lines correspond, respectively, to $|\mathbf{S}_{12}| = |R^{(-1,0)}|$, $|\mathbf{S}_{22}| = |R^{(0,0)}|$, and $|\mathbf{S}_{32}| = |R^{(+1,0)}|$. Analytical, numerical, and experimental results are given, respectively, by the solid lines, the dashed lines, and the symbols.

reflection at $\omega \pm \omega_m$ in response to an incidence at ω, i.e., $|\mathbf{S}_{32}| = |R^{(+1,0)}|$ and $|\mathbf{S}_{12}| = |R^{(-1,0)}|$.

Cosine modulation then generates both positive and negative Floquet harmonics [Figs. 3(a-1,3)] while a complex function, e.g., a positive (respectively negative) complex exponential, generates only positive (respectively negative) Floquet harmonics as evidenced in Fig. 3(a-1) [respectively Fig. 3(c-3)].

We compare the experimental results (circle symbols) with numerical simulation based on a finite-difference time-domain (FDTD) approach (dashed lines) and an analytical model based on a two-time-scale approach (solid lines). More details on the analytical and numerical modeling can be found in Appendix A. It is noteworthy here that these three methods require prior and accurate characterization of the loudspeaker and evaluation of its mechanical parameters (see Appendix A).

We can note a slight discrepancy just before the control frequency between the analytical model and the numerical and experimental results. This can be explained by the way the control bandwidth is applied. Indeed, both numerically and experimentally, a complex envelope technique involving second-order Bessel filtering is used, whereas the analytical modeling involves only a generalized normal distribution window (see Appendix A). Nevertheless, it is worth noting that the analytical model matches well with

the expected numerical and experimental reflection value at f_c, both at the fundamental and at the first positive and negative Floquet harmonics, thus validating our analytical modeling and the extraction procedure.

A detailed analysis of the effect of the modulation depth, target impedance, and modulation frequency can be found in Appendix B.

C. Broadband control

Extracting the full scattering matrix is only relevant if the time-modulated load is effective also at the frequency of the harmonics. Then, the generated harmonic, for example at $\omega \pm \omega_m$, generates back a Floquet harmonic that contributes to the reflection at ω, making the measurement more challenging.

A substantial incident amplitude at ω and $\omega \pm \omega_m$ is required to measure these backscatter coefficients, which correspond to the first and third columns of the scattering matrix in our case. Floquet harmonics then need to be generated by the time-modulated load for any incident frequency. In other words, the control has to be broadband and has to generate large-amplitude harmonics.

To do so, we change the control law applied to the system and modulate no longer the magnitude of the load impedance but its compliance C_{ms}, i.e., its resonance
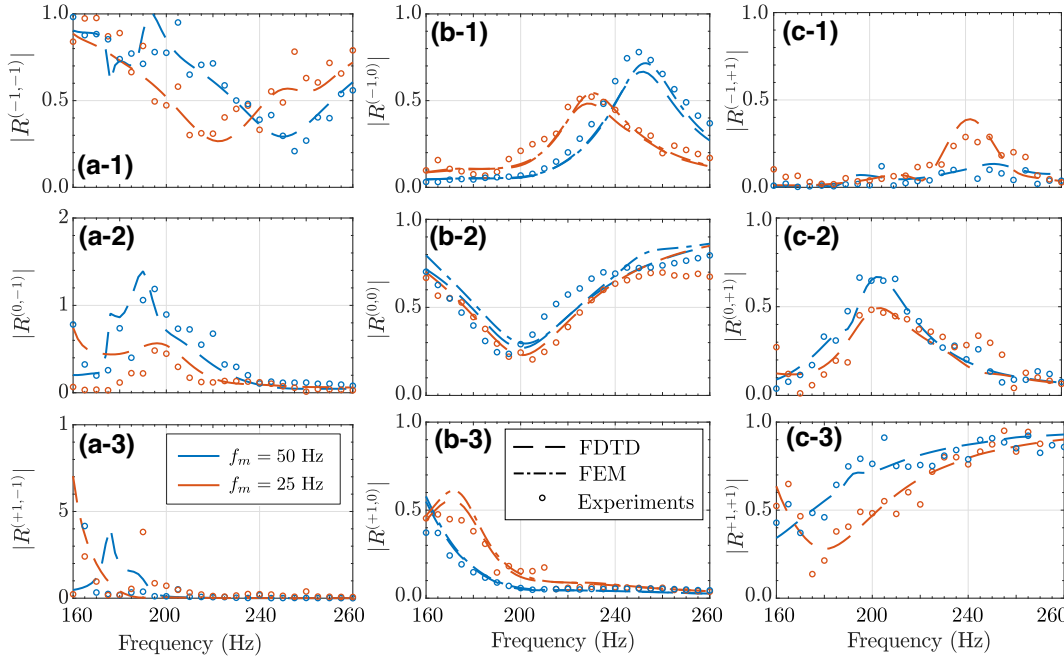
FIG. 4. Full scattering matrix of the time-modulated loudspeaker for a modulation $f_m = 50$ Hz (blue) or $f_m = 25$ Hz (red), $\phi_m = 0$, and $Z_{targ} = Z_{ms}(\omega) + 0.2(i\omega C_{ms}S_d^2)^{-1}\cos(\omega_m t + \phi_m)$. Reflection coefficient towards $\omega - \omega_m$ (1), towards ω (2), and towards $\omega + \omega_m$ (3) for incidence at $\omega - \omega_m$ (a), at ω (b), and at $\omega + \omega_m$ (c). Finite-element method (FEM) (only for the second column) and FDTD simulations are given, respectively, by the dashed-dotted and long-dashed lines. Experimental results are given by the circle symbols.

frequency,

$$Z_{targ}(\omega, t) = Z_{ms}(\omega) + (i\omega C_{ms}S_d^2)^{-1}A_m\cos(\omega_m t + \phi_m). \quad (28)$$

This new broadband control law still generates mostly one positive and one negative Floquet harmonics, but its stronger effect increases their amplitude, allowing the extraction of the complete $\mathbf{S}_t$ matrix.

Figure 4 shows two complete three-by-three scattering matrices obtained for two different modulation frequencies, $f_m = 50$ Hz (blue) and $f_m = 25$ Hz (red). The experimental results represented by the circle symbols are compared to the scattering coefficients extracted using the two-probe multiload technique applied to the FDTD experiment. To complement these two methods, a finite element method (FEM) model based on a Fourier expansion of the target impedance is also developed to validate the second column of the scattering matrix. Only the reflections for an incidence at the excitation frequency, i.e., second column only, is accessible with the FEM model (dashed-dotted line, see Appendix A for more details).

The first, second, and third columns of the scattering matrix [see Figs. 4(a)–4(c)] correspond, respectively, to reflection from incidence at $\omega - \omega_m$, ω, and $\omega + \omega_m$, to $\omega - \omega_m$, ω, and $\omega + \omega_m$ for the first, second, and third line elements [Figs. 4(1,2,3)].

The reflection at the excitation frequency is again that of the speaker with a drop in reflection at the natural resonant

frequency, i.e., 200 Hz for $|\mathbf{S}_{22}|$ in Fig. 4(b-2). Since the first and third columns refer to what happens at $\omega \pm \omega_m$, the reflection curve and the drop are therefore delocalized to 200 Hz $\pm f_m$ for $|\mathbf{S}_{33}|$ and $|\mathbf{S}_{11}|$, shown in Figs. 4(c-3) and 4(a-1), respectively.

The scattering coefficients of these two columns rely mainly on the incident pressures measured at $\omega \pm \omega_m$, which are uniquely due to the generated harmonics and are thus more sensitive to noise, hence the larger variance of the experimental data. Another source of discrepancies comes from the condition number of the matrix to be inverted, which depends on the chosen lengths of the multiloads and is optimal only for the center of the frequency range but not necessarily for all frequencies of the bandwidth. The difference in amplitude of the different off-diagonal terms is explained by the frequency dispersion of the speaker.

Except for the slight discrepancies for some frequencies, the overall agreement of the measured data with the simulation of the full experimental setup (including the dispersion and mechanical damping of the source) demonstrates the ability to measure the full scattering matrix of time-modulated systems.

V. CONCLUSIONS

In conclusion, we have studied the effect of a time-modulated load on a typical transmission line, and we have extended the classical theory to include the Floquet

harmonic generated by the system. We have tackled the challenge of experimentally characterizing the scattering of such structures, by implementing a multiload measurement technique. The characterization of time-modulated building blocks is an essential element for the design of more complex devices like space-time-varying metamaterials. The extended transmission-line theory and scattering extraction methodology are verified and applied to a one-dimensional acoustic transmission line terminated by a time-modulated load. To do so, we periodically modulated in time the input impedance of an actively controlled loudspeaker. The experimental scattering is confronted with both time-domain numerical simulations and analytical modeling based on a two-time-scale model of the controlled loudspeaker. The agreement of the three is very good for the different functions and modulation parameters tested. An interesting feature is the possibility to force the generation of either positive and/or negative Floquet harmonics solely by the choice of the modulation function applied in the control law. This unique behavior could be used to improve sound absorption by transferring low-frequency acoustic energy only to the higher harmonics, which can be absorbed more easily. In addition, to the extended telegrapher's equations, which could also be applied to the characterization of nonlinear load, we

also present an analytically well-described time-modulated controllable acoustic system which can be used in various applications of time-varying phenomena such as nonreciprocal devices, acoustic circulators, and non-Hermitian systems, among others.

APPENDIX A: DETAILS ON THE MODELING

1. Analytical model: two-time-scale method

The actively controlled loudspeaker follows an integrodifferential equation relating the velocity of the loudspeaker diaphragm $v(t)$ to the pressure in front of the loudspeaker $p_f(t)$,

$$\left(M_{\mathrm{ms}}d_{tt}^2 + R_{\mathrm{ms}}d_t + [C_{\mathrm{ms}}]^{-1}\right)v(t)$$
$$= S_d d_t p_f(t) - Bl\,d_t i(t) W(\omega), \qquad (A1)$$

where R_{ms}, M_{ms}, and C_{ms} are the Thiele and Small characteristics of the loudspeaker, i.e., acoustic resistance, mass, and compliance, respectively, and $W(\omega)$ is a frequency-generalized normal-distribution window centered at f_c.

Inserting Eq. (25) into Eq. (A1), imposing the change of variable $\tau = \omega_\infty t$ to obtain a dimensionless time variable, and rearranging the terms, we obtain

$$\left(d_{\tau\tau}^2 + \frac{R_{\mathrm{ms}}}{M_{\mathrm{ms}}\omega_\infty}d_\tau + 1\right)v(\tau) = \frac{S_d}{M_{\mathrm{ms}}\omega_\infty}d_\tau\left[1 - \left(1 - \frac{Z_{\mathrm{ms}}(\omega_c)}{Z_t\left(1 + A\cos\left((\omega_m/\omega_\infty)\tau + \phi_m\right)\right)}\right)W(\omega)\right]p_f(\tau), \qquad (A2)$$

with $\omega_\infty^2 = [C_{\mathrm{ms}}M_{\mathrm{ms}}]^{-1}$ the natural resonance circular frequency of the loudspeaker.

The system is excited by a source delivering a pressure $p(\tau) = P_{\mathrm{inc}}\exp\left(i\omega/\omega_\infty\tau\right)$. At $\tau = 0$ (initial condition), the driven loudspeaker has zero acceleration $d_\tau v(\tau)|_{\tau=0} = 0$ and has a velocity equal to $S_d v(\tau = 0) = p_f(\tau = 0)/Z_{\mathrm{ms}} = P_{\mathrm{inc}}/Z_{\mathrm{ms}}$.

We assume that the system can be described using two different time scales: one related to the excitation at ω, $T_0 \approx \tau$, and the other related to the slow modulation at ω_m,

$T_1 \approx \epsilon\tau$, such that $T_0 \gg T_1$. We define a small parameter for the derivations, $\epsilon \approx \omega_m/\omega_\infty \ll 1$. We also note that the prefactor on the right-hand side of Eq. (A2) is of the same order as ϵ, so $S_d/M_{\mathrm{ms}}\omega_\infty$ can be replaced by $\epsilon S_d/M_{\mathrm{ms}}\omega_m$.

The velocity field can then be extended according to these two scales:

$$v(\tau) \approx v_0(T_0, T_1) + \epsilon v_1(T_0, T_1). \qquad (A3)$$

The governing equation can then be rewritten as

$$\left(\partial_{T_0 T_0}^2 + 2\epsilon\partial_{T_0 T_1}^2 + \epsilon^2\partial_{T_1 T_1}^2 + \frac{R_{\mathrm{ms}}}{M_{\mathrm{ms}}\omega_\infty}\partial_{T_0} + \frac{R_{\mathrm{ms}}}{M_{\mathrm{ms}}\omega_\infty}\epsilon\partial_{T_1} + 1\right)(v_0(T_0, T_1) + \epsilon v_1(T_0, T_1))$$
$$= \epsilon\frac{S_d}{M_{\mathrm{ms}}\omega_m}(\partial_{T_0} + \epsilon\partial_{T_1})\left[1 - \left(1 - \frac{Z_{\mathrm{ms}}(\omega_c)}{Z_t\left(1 + A\cos\left(T_1 + \phi_m\right)\right)}\right)W(\omega)\right]p_f(T_0). \qquad (A4)$$

Separating the different orders in ϵ, we get

$$\mathcal{O}(\epsilon^0) \rightarrow \left(\partial^2_{T_0 T_0} + \frac{R_{\mathrm{ms}}}{M_{\mathrm{ms}}\omega_\infty}\partial_{T_0} + 1\right) v_0 = 0, \tag{A5}$$

$$\mathcal{O}(\epsilon^1) \rightarrow \left(\partial^2_{T_0 T_0} + \frac{R_{\mathrm{ms}}}{M_{\mathrm{ms}}\omega_\infty}\partial_{T_0} + 1\right) v_1 = \frac{S_d}{M_{\mathrm{ms}}\omega_m}\partial_{T_0}\left[1 - \left(1 - \frac{Z_{\mathrm{ms}}(\omega_c)}{Z_t\left(1 + A\cos\left(T_1 + \phi_m\right)\right)}\right) W(\omega)\right] p_f(T_0)$$
$$- \left(2\partial^2_{T_0 T_1} + \frac{R_{\mathrm{ms}}}{M_{\mathrm{ms}}\omega_\infty}\partial_{T_1}\right) v_0. \tag{A6}$$

To solve the governing equation of the loudspeaker, we now have to solve each of the two separated partial differential equations giving the solution at orders zero and one, v_0 and v_1, respectively. We first solve the partial differential equation at order zero, Eq. (A5), using the initial conditions. We then reinject the solution v_0 into Eq. (A6) and cancel the secular terms, to obtain the solution v_1.

Finally, using the definition of the velocity-field expansion, Eq. (A3), remembering that the two time scales are $T_0 \approx \tau$ and $T_1 \approx \epsilon\tau$, and replacing ϵ and τ by their definitions, we can derive the total solution to the initial governing equation, Eq. (A1):

$$v(t) = \frac{P_{\mathrm{inc}}}{S_d Z_{\mathrm{ms}}} e^{-(R_{\mathrm{ms}}/2M_{\mathrm{ms}})t} \cos\left(\sqrt{1 - \left(\frac{R_{\mathrm{ms}}}{2M_{\mathrm{ms}}\omega_\infty}\right)^2}\omega_\infty t\right) + \frac{P_{\mathrm{inc}}}{S_d Z_{\mathrm{ms}}}\left[1 - \left(1 - \frac{Z_{\mathrm{ms}}(\omega_c)}{Z_t\left(1 + A\cos\left(\omega_m t + \phi_m\right)\right)}\right) W(\omega)\right] e^{i\omega t}. \tag{A7}$$

The first term corresponds to the transient field and decays exponentially with the speaker dissipation constant $R_{\mathrm{ms}}/2M_{\mathrm{ms}}$. At the control frequency, the loudspeaker responds effectively to the target impedance, $v(t) = P_{\mathrm{inc}}/\left(S_d Z_t\left(1 + A\cos\left(\omega_m t + \phi_m\right)\right)\right)$. A constant fitting parameter is introduced such that $A = A_m/2$.

To extract the impedance matrix **Z** from the analytical model, we have to use the superposition principle and solve the system for an incident pressure at ω, $\omega - \omega_m$, and $\omega + \omega_m$, and for $2N + 1$ charges. Then, the Fourier transform of the pressure and velocity fields allows us to solve Eq. (22) and thus to derive the scattering matrix equation (13).

2. Numerical FDTD model

Numerical results are obtained using SIMULINK modeling of the entire experimental setup, based on a finite-difference time step approach using a time step of 10^{-5}. The scattering and impedance matrices can then be extracted from the incident and reflected pressures, using the two-probe multiload technique applied to the numerical experiment. The results obtained via the extraction procedure performed as in the experimental setup are consistent with those obtained from the direct access to the reflected and transmitted pressures allowed by the simulation.

3. Numerical FEM model

The numerical FEM experiment is performed using the frequency-domain solver of the commercial software COMSOL Multiphysics, following the methodology proposed in Ref. [10]. The time-modulated loudspeaker is modeled as an impedance,

$$Z = Z_{\mathrm{ms}}(\omega) + A_m[i\omega C_{\mathrm{ms}}S_d^2]^{-1}\cos(\omega_m t + \phi_m) \tag{A8}$$

$$= Z_{\mathrm{ms}}(\omega) + \delta Z(\omega)(e^{i\omega_m t}e^{i\phi_m} + e^{-i\omega_m t}e^{-i\phi_m}). \tag{A9}$$

An impedance condition is implemented as follows:

$$-\mathbf{n}\frac{\nabla p}{\rho_0} = p_f\frac{-i\omega}{Z} = -\mathbf{v}\cdot\mathbf{n}\,i\omega. \tag{A10}$$

Expanding p_f and v (normal particle velocity) in Fourier series, after some algebra we end up with

$$p_{f_n} = Z(\omega_n)v_n + \delta Z(\omega_n)\left(v_{n-1}e^{-i\phi_m} + v_{n+1}e^{i\phi_m} + \cdots\right), \tag{A11}$$

or equivalently

$$v_n = \frac{p_{f_n} - \delta(\omega_n)\left(v_{n-1}e^{-i\phi_m} + v_{n+1}e^{i\phi_m} + \cdots\right)}{Z(\omega_n)}, \tag{A12}$$

where $\omega_n = \omega + n\omega_m$.

We then put Eq. (A12) into weak forms and solve for $n = (-2, -1, 0, 1, 2)$ simultaneously for any incident frequency ω.

4. Characterization of the resonator to control

A fitting procedure of the transfer function of the loudspeaker terminated by an open circuit, a short circuit, or a load $R = 100.8 \ \Omega$, allows the following Thiele and Small parameters [56] to be obtained: $Bl = 3.63$ T m, $M_{ms} = 2.9$ g, $C_{ms} = 0.214$ mm/N, and $R_{ms} = 0.54$ N s/m. The natural resonance of the speaker occurs close to 200 Hz. We thus choose to apply our control around the resonance to take advantage of the stable response in this range

APPENDIX B: EFFECT AND LIMITATION OF THE CONTROL CHARACTERISTICS

1. Change of the control frequency

Figure 5 shows three configurations with positive circular modulation and control frequency on either side of the natural resonance frequency, i.e., $f_c = 180$ Hz (a), $f_c = 220$ Hz (b) and $f_c = 260$ Hz (c). It can be seen that the active control does capture the reflection value $|R^{(0,0)}| = 0.11$ for each of the control frequencies, and that a $+1$ Floquet harmonic is generated. The amplitude of the latter differs depending on the control frequency, again, due to the dispersion of the electrodynamic speaker.

2. Change of the target impedance $\tilde{Z}_t$

We then test in Fig. 6 three different target impedance values, respectively, $\tilde{Z}_t = 0.4$ (a), $\tilde{Z}_t = 0.6$ (b), and $\tilde{Z}_t = 1$
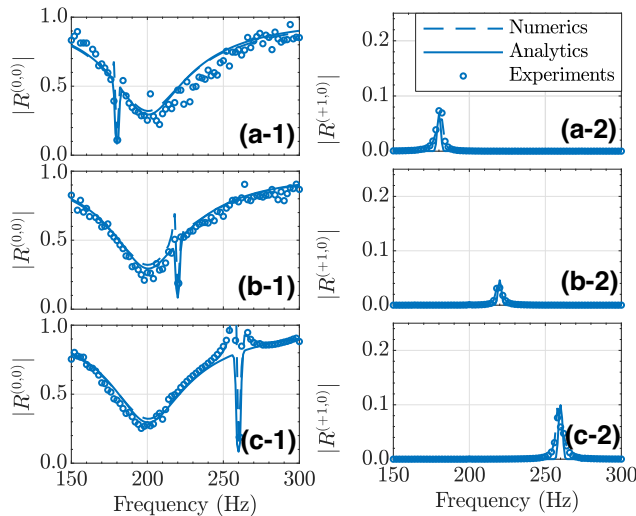

FIG. 5. Control frequency f_c variation: (a) $f_c = 180$ Hz, (b) $f_c = 220$ Hz, and (c) $f_c = 260$ Hz for the fundamental $|R^{(0,0)}|$ (1) and the first Floquet harmonic $|R^{(+1,0)}|$ (2). Analytical, numerical, and experimental results are given, respectively, by the solid lines, the dashed lines, and the symbols.
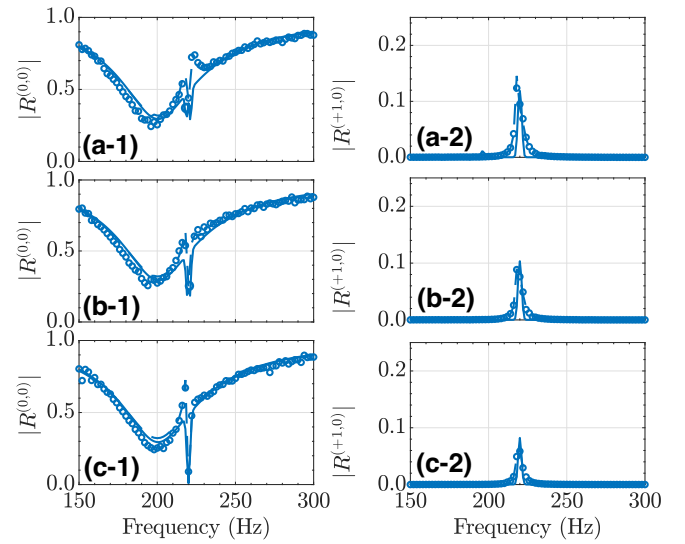

FIG. 6. Target impedance $\tilde{Z}_t$ variation: (a) $\tilde{Z}_t = 0.4$, (b) $\tilde{Z}_t = 0.6$, and (c) $\tilde{Z}_t = 1$ for the fundamental $|R^{(0,0)}|$ (1) and the first Floquet harmonic $|R^{(+1,0)}|$ (2). Analytical, numerical, and experimental results are given, respectively, by the solid lines, the dashed lines, and the symbols.

(c). Here, again, the agreement between the three methods is rather good. The reflection at ω falls to $|R^{(0,0)}| = 0.28$, $|R^{(0,0)}| = 0.25$, and $|R^{(0,0)}| = 0$, respectively, for $\tilde{Z}_t = 0.4$, $\tilde{Z}_t = 0.6$, and $\tilde{Z}_t = 1$. The smaller the impedance, the larger the reflection at both ω and $\omega + \omega_m$. Furthermore, it should be noted here that, even though, for $\tilde{Z}_t = 1$, we have an impedance matching and thus $|R^{(0,0)}| = 0$, a reflection at $\omega + \omega_m$ exists, $|R^{(+1,0)}| \neq 0$. The termination load is only impedance-matched at the control frequency f_c but not at $f_c + f_m$; in other words, $\mathbf{Z}_t(1, 2) \neq Z_0$. A point where vigilance is required is that the control may be limited by instabilities if the loudspeaker is asked to respond with an impedance too different from its natural impedance at a given frequency.

3. Change of the modulation depth A_m

Finally, we study the effect of changing the modulation amplitude, also called modulation depth. We assign three different values, $A_m = 0$, $A_m = 0.4$, and $A_m = 0.6$, as illustrated in Figs. 7(a)–7(c), respectively.

As anticipated, the modulation depth has almost no impact on the reflection at the fundamental frequency. For zero modulation depth, Fig. 7(a), i.e., a time-invariant control, no Floquet harmonics are generated. Furthermore, the higher the modulation depth, the higher the magnitude of the reflection at the first Floquet harmonic $|R^{(+1,0)}|$. A point of caution with the variation of A_m should be noted: a high modulation depth can also generate higher-order harmonics. It is therefore important to check the magnitude of the
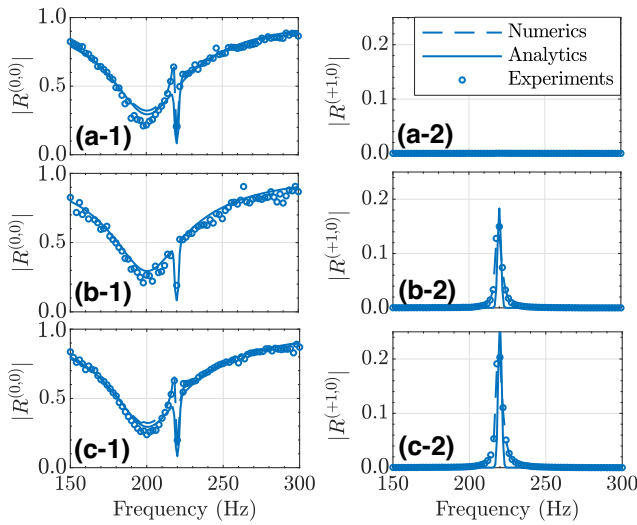
FIG. 7. Modulation depth A_m variation: (a) $A_m = 0$, (b) $A_m = 0.4$, and (c) $A_m = 0.6$ for the fundamental $|R^{(0,0)}|$ (1) and the first Floquet harmonic $|R^{(+1,0)}|$ (2). Analytical, numerical, and experimental results are given, respectively, by the solid lines, the dashed lines, and the symbols.

reflection at $\omega + n\omega_m$, and, if necessary, adapt the dimension of the **S** matrix to account for the additional harmonics in the calculation.

APPENDIX C: DETAILS ON THE EXPERIMENTAL SETUP

The acoustic apparatus used for the characterization of **S** and illustrated in Fig. 2 consists of an acoustic waveguide made up of removable portions of a 7.18-cm-diameter circular duct, terminated on one side by an electrodynamic loudspeaker (Monacor SPX-30 M, 3 in.) acting as the source, and on the other side by the time-modulated load. To consider only the propagation of plane waves, we take care to work only below the first cutoff frequency of the waveguide ($f_c = 1.8412c_0/2\pi a = 1400$ Hz).

The time-modulated load is an actively controlled electrodynamic loudspeaker (Monacor SPX-30 M, 3 in.) enclosed in a cavity of volume $V_b = 1081.6$ cm³ and instrumented with an integrated circuit piezoelectric (ICP) microphone (PCB 130F20, 1/4 in.) placed just in front of the loudspeaker diaphragm. The active control scheme as well as the excitation signal generation and data acquisition are performed with an FPGA-based Speedgoat Performance real-time controller (I/O 131) controlled by the MATLAB/SIMULINK xPC target environment. The controller's output voltage is converted by a homemade voltage-to-current converter (0.2083 A/V) based on a Howland pump circuit and fed into the controlled speaker.

The incident and reflected pressures are derived from the pressure measured by two ICP microphones (PCB 130F20, 1/4 in.) 24 cm apart and 5 cm from the excitation source.

To characterize the full scattering matrix, a multicharge technique is used, with $L_{\text{load}} = 50$, 62.5, and 87.5 cm, respectively, thus ensuring a consistent difference in phase delay due to the round-trip propagation distance between the microphones and time-modulated load for each configuration. It is important to note that the distance should be chosen according to the center frequency of the bandwidth under consideration. Note that a further extension to multimode characterization is possible, but will require an increased number of sensors.

[1] E. Galiffi, R. Tirole, S. Yin, H. Li, S. Vezzoli, P. A. Huidobro, M. G. Silveirinha, R. Sapienza, A. Alù, and J. B. Pendry, Photonics of time-varying media, Adv. Photonics **4**, 014002 (2022).

[2] F. Morgenthaler, Velocity modulation of electromagnetic waves, IEEE Trans. Microw. Theory Tech. **6**, 167 (1958).

[3] L. Felsen and G. Whitman, Wave propagation in time-varying media, IEEE Trans. Antennas Propag. **18**, 242 (1970).

[4] R. Fante, Transmission of electromagnetic waves into time-varying media, IEEE Trans. Antennas Propag. **19**, 417 (1971).

[5] T. T. Koutserimpas and R. Fleury, Electromagnetic waves in a time periodic medium with step-varying refractive index, IEEE Trans. Antennas Propag. **66**, 5300 (2018).

[6] S. Yin, E. Galiffi, and A. Alu, Floquet metamaterials, eLight **2**, 8 (2022).

[7] D. L. Sounas and A. Alu, Non-reciprocal photonics based on time modulation, Nat. Photonics **11**, 774 (2017).

[8] Y. Hadad, in *2020 14th European Conference on Antennas and Propagation (EuCAP)* (2020).

[9] J. Li, Y. Jing, and S. A. Cummer, Nonreciprocal coupling in space-time modulated systems at exceptional points, Phys. Rev. B **105**, L100304 (2022).

[10] R. Fleury, D. L. Sounas, and A. Alu, Subwavelength ultrasonic circulator based on spatiotemporal modulation, Phys. Rev. B **91**, 174306 (2015).

[11] V. Pacheco-Peña and N. Engheta, Temporal aiming, Light: Sci. Appl. **9**, 129 (2020).

[12] M. C. Rechtsman, J. M. Zeuner, Y. Plotnik, Y. Lumer, D. Podolsky, F. Dreisow, S. Nolte, M. Segev, and A. Szameit, Photonic Floquet topological insulators, Nature **496**, 196 (2013).

[13] R. Fleury, A. B. Khanikaev, and A. Alu, Floquet topological insulators for sound, Nat. Commun. **7**, 11744 (2016).

[14] Z. Zhang, P. Delplace, and R. Fleury, Superior robustness of anomalous non-reciprocal topological edge states, Nature **598**, 293 (2021).

[15] W. Zhu, H. Xue, J. Gong, Y. Chong, and B. Zhang, Time-periodic corner states from Floquet higher-order topology, Nat. Commun. **13**, 11 (2022).

[16] A. L. CULLEN, A travelling-wave parametric amplifier, Nature **181**, 332 (1958).

[17] T. T. Koutserimpas and R. Fleury, Nonreciprocal Gain in Non-Hermitian Time-Floquet Systems, Phys. Rev. Lett. **120**, 087401 (2018).

[18] T. T. Koutserimpas, A. Alu, and R. Fleury, Parametric amplification and bidirectional invisibility in PT-symmetric time-Floquet systems, Phys. Rev. A **97**, 013839 (2018).

[19] A. Y. Song, Y. Shi, Q. Lin, and S. Fan, Direction-dependent parity-time phase transition and nonreciprocal amplification with dynamic gain-loss modulation, Phys. Rev. A **99**, 013824 (2019).

[20] J. Li, C. Shen, X. Zhu, Y. Xie, and S. A. Cummer, Nonreciprocal sound propagation in space-time modulated media, Phys. Rev. B **99**, 144311 (2019).

[21] C. Shen, X. Zhu, J. Li, and S. A. Cummer, Nonreciprocal acoustic transmission in space-time modulated coupled resonators, Phys. Rev. B **100**, 054302 (2019).

[22] C. Shen, J. Li, Z. Jia, Y. Xie, and S. A. Cummer, Nonreciprocal acoustic transmission in cascaded resonators via spatiotemporal modulation, Phys. Rev. B **99**, 134306 (2019).

[23] X. Zhu, J. Li, C. Shen, G. Zhang, S. A. Cummer, and L. Li, Tunable unidirectional compact acoustic amplifier via space-time modulated membranes, Phys. Rev. B **102**, 024309 (2020).

[24] X. Zhu, J. Li, C. Shen, X. Peng, A. Song, L. Li, and S. A. Cummer, Non-reciprocal acoustic transmission via space-time modulated membranes, Appl. Phys. Lett. **116**, 034101 (2020).

[25] X. Wen, X. Zhu, A. Fan, W. Y. Tam, J. Zhu, H. W. Wu, F. Lemoult, M. Fink, and J. Li, Unidirectional amplification with acoustic non-hermitian space-time varying metamaterial, Commun. Phys. **5**, 18 (2022).

[26] K. Lee, J. Son, J. Park, B. Kang, W. Jeon, F. Rotermund, and B. Min, Linear frequency conversion via sudden merging of meta-atoms in time-variant metasurfaces, Nat. Photonics **12**, 765 (2018).

[27] J. Zhao, X. Yang, J. Y. Dai, Q. Cheng, X. Li, N. H. Qi, J. C. Ke, G. D. Bai, S. Liu, S. Jin, A. Alu, and T. J. Cui, Programmable time-domain digital-coding metasurface for non-linear harmonic manipulation and new wireless communication systems, Natl. Sci. Rev. **6**, 231 (2019).

[28] V. Bacot, M. Labousse, A. Eddi, M. Fink, and E. Fort, Time reversal and holography with space-time transformations, Nat. Phys. **12**, 972 (2016).

[29] S. Vezzoli, V. Bruno, C. DeVault, T. Roger, V. M. Shalaev, A. Boltasseva, M. Ferrera, M. Clerici, A. Dubietis, and D. Faccio, Optical Time Reversal from Time-Dependent Epsilon-Near-Zero Media, Phys. Rev. Lett. **120**, 043902 (2018).

[30] T. T. Koutserimpas and R. Fleury, Zero refractive index in time-Floquet acoustic metamaterials, J. Appl. Phys. **123**, 091709 (2018).

[31] Y. Yang, J. Lu, A. Manjavacas, T. S. Luk, H. Liu, K. Kelley, J.-P. Maria, E. L. Runnerstrom, M. B. Sinclair, S. Ghimire, and I. Brener, High-harmonic generation from an epsilon-near-zero material, Nat. Phys. **15**, 1022 (2019).

[32] V. Bruno, C. DeVault, S. Vezzoli, Z. Kudyshev, T. Huq, S. Mignuzzi, A. Jacassi, S. Saha, Y. D. Shah, S. A. Maier, D. R. S. Cumming, A. Boltasseva, M. Ferrera, M. Clerici, D. Faccio, R. Sapienza, and V. M. Shalaev, Negative Refraction in Time-Varying Strongly Coupled Plasmonic-Antenna–Epsilon-Near-Zero Systems, Phys. Rev. Lett. **124**, 043902 (2020).

[33] Y. Zhou, M. Z. Alam, M. Karimi, J. Upham, O. Reshef, C. Liu, A. E. Willner, and R. W. Boyd, Broadband frequency translation through time refraction in an epsilon-near-zero material, Nat. Commun. **11**, 2180 (2020).

[34] J.-Y. Shan, M. Ye, H. Chu, S. Lee, J.-G. Park, L. Balents, and D. Hsieh, Giant modulation of optical nonlinearity by Floquet engineering, Nature **602**, E19 (2022).

[35] S. Mukherjee and M. C. Rechtsman, Observation of Floquet solitons in a topological bandgap, Science **368**, 856 (2020).

[36] A. Momeni and R. Fleury, Electromagnetic wave-based extreme deep learning with nonlinear time-Floquet entanglement, Nat. Commun. **13**, 2651 (2022).

[37] V. Pacheco-Peña and N. Engheta, Effective medium concept in temporal metamaterials, Nanophotonics **9**, 379 (2020).

[38] C. Rizza, G. Castaldi, and V. Galdi, Nonlocal effects in temporal metamaterials, Nanophotonics **11**, 1285 (2022).

[39] P. Jayathurathnage, F. Liu, M. S. Mirmoosa, X. Wang, R. Fleury, and S. A. Tretyakov, Time-Varying Components for Enhancing Wireless Transfer of Power and Information, Phys. Rev. Appl. **16**, 014017 (2021).

[40] D. M. Solís and N. Engheta, Functional analysis of the polarization response in linear time-varying media: A generalization of the kramers-kronig relations, Phys. Rev. B **103**, 144303 (2021).

[41] M. S. Mirmoosa, T. T. Koutserimpas, G. A. Ptitcyn, S. A. Tretyakov, and R. Fleury, Dipole polarizability of time-varying particles, New J. Phys. **24**, 063004 (2022).

[42] J. Li, X. Zhu, C. Shen, X. Peng, and S. A. Cummer, Transfer matrix method for the analysis of space-time-modulated media and systems, Phys. Rev. B **100**, 144311 (2019).

[43] P. Garg, A. G. Lamprianidis, D. Beutel, T. Karamanos, B. Verfürth, and C. Rockstuhl, Modeling four-dimensional metamaterials: A T-matrix approach to describe time-varying metasurfaces, Opt. Express **30**, 45832 (2022).

[44] M. B. Steer, *Microwave and RF Design* (NC State University, Raleigh, North Carolina, 2019).

[45] A. Sitel, J.-M. Ville, and F. Foucart, Multiload procedure to measure the acoustic scattering matrix of a duct discontinuity for higher order mode propagation conditions, J. Acoust. Soc. Am. **120**, 2478 (2006).

[46] T. T. Koutserimpas, E. Rivet, H. Lissek, and R. Fleury, Active Acoustic Resonators with Reconfigurable Resonance Frequency, Absorption, and Bandwidth, Phys. Rev. Appl. **12**, 054064 (2019).

[47] G. Penelet, V. Pagneux, G. Poignand, C. Olivier, and Y. Aurégan, Broadband Nonreciprocal Acoustic Scattering Using a Loudspeaker with Asymmetric Feedback, Phys. Rev. Appl. **16**, 064012 (2021).

[48] R. Fleury, D. Sounas, and A. Alu, An invisible acoustic sensor based on parity-time symmetry, Nat. Commun. **6**, 5905 (2015).

[49] E. Rivet, A. Brandstötter, K. G. Makris, H. Lissek, S. Rotter, and R. Fleury, Constant-pressure sound waves in non-Hermitian disordered media, Nat. Phys. **14**, 942 (2018).

[50] M. Furstoss, D. Thenail, and M. Galland, Surface impedance control for sound absorption: Direct and

hybrid passive/active stategies, J. Sound Vib. **203**, 219 (1997).

[51] M. Collet, P. David, and M. Berthillier, Active acoustical impedance using distributed electrodynamical transducers, J. Acoust. Soc. Am. **125**, 882 (2009).

[52] H. Lissek, R. Boulandet, and R. Fleury, Electroacoustic absorbers: Bridging the gap between shunt loudspeakers and active sound absorption, J. Acoust. Soc. Am. **129**, 2968 (2011).

[53] E. Rivet, S. Karkar, and H. Lissek, Broadband low-frequency electroacoustic absorbers through hybrid sensor-shunt-based impedance control, IEEE Trans. Control Syst. Technol. **25**, 63 (2017).

[54] X. Guo, H. Lissek, and R. Fleury, Improving Sound Absorption Through Nonlinear Active Electroacoustic Resonators, Phys. Rev. Appl. **13**, 014018 (2020).

[55] X. Guo, M. Volery, and H. Lissek, PID-like active impedance control for electroacoustic resonators to design tunable single-degree-of-freedom sound absorbers, J. Sound Vib. **525**, 116784 (2022).

[56] R. H. Small, Closed-box loudspeaker systems – part 1: Analysis, J. Audio Eng. Soc. **20**, 798 (1972).